

# Measuring pore water velocities and dynamic contact angles at unstable wetting fronts

Naaran Brindt, Xinying Min, Jiuzhou Yan, Sunghwan Jung, J-Yves Parlange, Tammo S. Steenhuis\*

*Department of Biological and Environmental Engineering, Cornell University, 206 Riley Robb Hall, Ithaca, NY 14853, United States*



## ARTICLE INFO

**Keywords:**  
Fingers  
Vadose zone  
Preferential flow  
Sand  
Instability  
Critical zone

## ABSTRACT

The imbibition of fluids in porous media has been studied widely. Still, processes of preferential flow under gravity due to instability at the wetting front, crucial in groundwater contamination, have yet to be fully understood. Recent theories using dynamic contact angles could describe unstable flow phenomena but have not been proven experimentally. Therefore, infiltration experiments in small sand-filled chambers were conducted to explore the effect of dynamic contact angles. A high-speed camera recorded pore invasion at the unstable imbibition liquid front. A tensiometer recorded the matric potential. The results show that water moved in milliseconds through a small pore at the wetting front, followed by a stationary period. The maximum observed pore water velocity was 25 cm/s, exceeding the saturated hydraulic conductivity by three orders of magnitude. The relationship between dynamic contact angle and water velocity found by Hoffman in glass tubes could describe which was observed in soils.

## 1. Introduction

Imbibition, where a wetting fluid enters a porous medium and displaces an *in-situ* fluid, has been studied widely for over 150 years. Initially, it was investigated to quantify the loss of nitrogen fertilizer through drainage tile lines (Lawes et al., 1882) and for artificially draining soils (Wheeler, 1893). Currently, research on imbibition is performed widely to analyze natural and industrial processes such as gas and oil recovery from underground reservoirs (Esfandyari et al., 2021; Li et al., 2022), inkjet printing (Wijshoff, 2018), groundwater pollution and root water uptake (Sprenger et al., 2016; Miyata et al., 2010; Jarvis et al., 2008; Aslam et al., 2018), and stormwater harvesting using dry wells (Sasidharan et al., 2019).

According to several researchers (Li et al., 2022; Bakhshian et al., 2021; Morbidelli et al., 2018; Vereecken et al., 2019; Nimmo, 2021), imbibition in the presence of gravity is not entirely understood. In unsaturated soils, under gravity with surface water application, the wetting front moves down either as compact flow (also known as piston flow and stable displacement), which is described, among others, by Green and Ampt (1911), Klute (1952), and Gardner and Mayhugh (1958), or as preferential flow in columns (Starr et al., 1978; Andreini and Steenhuis, 1990). In compact flow, the water content and matric potential increase

monotonically above the front (Green and Ampt, 1911; Klute, 1952; Gardner and Mayhugh, 1958). Thus, the moisture content is greatest at the surface and least at the wetting front.

Preferential flow is caused by highly conductive pathways (such as wormholes) or unstable gravity-driven flow in uniform soils. These preferential flow paths rapidly transport some surface-applied chemicals to the groundwater, bypassing most of the soil matrix without adsorbing to the soil and with minimal breakdown. For pesticides that are toxic at concentrations of parts per billion, the amount transported downwards can be sufficient to contaminate the groundwater.

For both types of preferential flow, rainfall is distributed from a nearly saturated surface layer to preferential flow paths below. The preferential flow paths bypass most of the matrix of homogeneous sandy or water-repellent soils. They are known as fingers or columns (Hill and Parlange, 1972; Selker et al., 1992a; Dicarlo, 2004). For unstable, gravity-driven flow, the tip of these fingers is near saturation, and the water content and matric potential decrease above the front (Parlange et al., 2002; Geiger and Durnford, 2000; Egorov et al., 2003; Brindt et al., 2023).

The unstable gravity-driven flow in the finger behind the wetting front has been described well by using Richards' equation with the wetting front at the fingertip moving with a constant velocity at a

\* Corresponding author.

E-mail address: [tss1@cornell.edu](mailto:tss1@cornell.edu) (T.S. Steenhuis).

prescribed matric potential (Selker et al., 1992a; Brindt and Wallach, 2017, 2020; Kmec et al., 2019, 2021). However, the physics of the movement of the front is not understood. As a result, many diverse approaches have been proposed, such as perturbing the wetting front (Parlange and Hill, 1976), adding terms to the Richards' equation (Cuesta et al., 2000; Eliassi and Glass, 2003; Nieber et al., 2005; Cue-to-Felgueroso and Juanes, 2008; Hilpert, 2012), rule-based pore scales models (Glass and Yarrington, 2003), or with semi continuum methodologies (Brindt and Wallach, 2020). In addition, Lattice Boltzmann approaches are common in oil recovery studies, assuming capillary forces dominate gravitational forces. Only (Li et al., 2022) included gravity and (Bakhshian et al., 2021) wettability effects in the Lattice Boltzmann simulations. Gravity and wettability effects are critical for simulating unstable wetting fronts in unsaturated soils.

Beatty and Smith (2013), Wang and Wallach (2021, 2022), Hilpert (2012), Li et al. (2022) Brindt and Wallach (2017, 2020) employed dynamic contact angles (i.e., velocity-dependent contact angle) at the wetting front. These approaches were able to simulate the increased matric potential at the wetting front. However, they did not explain the physics of the increase. To provide a physical basis, Steenhuis et al. (2013) and Baver et al. (2014) posed that matric potential at the wetting front was discontinuous and the water advances through one pore at a time resulting in higher pore velocities than if all pores at the front would transport the imposed flux downwards. Since the matric potential was independent of the dry soil below, the greater velocity, in turn, increases the contact angle, as shown experimentally by Hoffman (1975), Baver et al. (2014), and Kim et al. (2017). Although the dynamic contact angle findings of Hoffman have been applied to the spreading of the contact line of droplets and sinking spheres (McHale et al., 2009; Kim et al., 2017), the phenomenon has not been shown to occur yet experimentally in soils.

Hoffman (1975) measured the advancing dynamic contact angle in horizontal capillary tubes using a moving steel plunger and five liquids with different static angles ( $\theta_s$ ) and viscosities. Jiang et al. (1979) fitted a nonlinear regression equation through the experimental data of Hoffman (1975) of the form,

$$\frac{\cos\theta_s - \cos\theta_d}{\cos\theta_s + 1} = \tanh(4.96 \text{ Ca}^{0.702}) \quad (1)$$

where  $\theta_s$  is the static contact angle,  $\theta_d$  is the dynamic contact angle, 4.96 and 0.702 are constants, and Ca is the capillary number given by:

$$\text{Ca} = \frac{\mu v}{\gamma} \quad (2)$$

where  $\mu$  is the dynamic viscosity of the liquid (Pa s),  $v$  is the velocity (m/s), and  $\gamma$  is the surface tension (N/m). Based on Eq. (1), the dynamic contact angle for a zero contact for the Hoffman data angle can be written as

$$\cos\theta_d^0 = 1 - 2\tanh(4.96 \text{ Ca}^{0.702}) \quad (3)$$

where  $\theta_d^0$  is the dynamic contact angle when the static contact angle is zero.

Physics dictates that the dynamic contact angle at  $180^\circ$  must equal the dynamic contact angle for zero static contact angle expressed in Eq. (3), viz.,

$$\theta_d^0 = \theta_d, \text{ for } \theta_d = 0 \text{ and } \theta_d = \pi \quad (4)$$

It can be easily checked that the Jiang Equation (Eq. (1)) meets the conditions in Eq. (4).

Baver et al. (2014) measured dynamic contact angles with five liquids under gravity with slug experiments with tubes at different slopes. The capillary numbers ranged from  $5 \cdot 10^{-3}$  to  $0.8 \cdot 10^{-1}$  with dynamic contact angles between  $40^\circ$  and  $140^\circ$ . They found that their measured dynamic contact angles fitted the Hoffman curve as expressed by Jiang

(Eq. (3)) when the static contact angles were zero. However, the Jiang equation (Eq. (1)) did not fit well for other dynamic contact angles at non-zero static contact angles. To improve the fit of the measured dynamic contact angles,  $\theta_d$  for non-zero static contact angles, they introduced the following function,

$$\theta_d = \theta_d^0 \frac{\pi - \theta_s}{\pi} + \theta_s \quad (5)$$

Eq. (5) has the same desired properties as the Jiang (1979) formulation, such that the original Hoffman curve is obtained when the static contact angle,  $\theta_s$ , is equal to zero. In addition, when the measured dynamic contact angle is equal to 0 and  $180^\circ$ , Eq. (4) is satisfied.

Substituting Eqs. (2) and (5) into Eq. (3) results in the Hofmann-Baver equation that specifies the dynamic contact angles as a function of all static contact angles, pore water velocity, dynamic viscosity and surface tension (Baver et al., 2014; Steenhuis et al., 2013)

$$\theta_d = \theta_s + \left(1 - \frac{\theta_s}{\pi}\right) \arccos \left[ 1 - 2\tanh \left( 4.96 \left( \frac{\mu v}{\gamma} \right)^{0.702} \right) \right] \quad (6)$$

Several other studies have experimentally examined the water/air interface at the pore scale in sands during imbibition or drainage. One study by Moebius and Or (2012) had the required spatial and temporal resolution to capture the dynamics of pore invasion during drainage. Using a high-speed camera and pressure sensor, they tracked water movement in Hele-Shaw cells with fritted glass beads. That study observed the rapid interface movements, also called Haynes jumps, associated with high flow velocity and pressure changes during drainage. Other studies that used high-speed photography were concerned with the rapid pore filling during drainage (Aker et al., 2000; Armstrong et al., 2015; Moebius and Or, 2012; Soto et al., 2017; Sun and Santamarina, 2019), pore filling in horizontal chambers or compact upward flow (Sun et al., 2016; Li et al., 2022), slug flow in a capillary (Nissan et al., 2016), pore water velocity during drop impact (Bouchard and Chandra, 2020), and evaporation (Haines, 1928; Mielniczuk and Huecke, 2022). Synchrotron X-rays were used by Berg et al. (2013), Kim et al. (2022), and Spurin et al. (2020) to document Haynes jumps during drainage. However, this synchrotron X-ray technique measured the moisture contents in seconds and could not accurately measure the velocities of pore invasions that occurred in milliseconds. Thus, none of the above studies looked in detail experimentally at pore invasions under gravity. So, the validity of changes in dynamic contact angles (as shown by Hoffman 1975), previously measured in plastic tubes, during imbibition has not been demonstrated experimentally to happen in concert with finger formation.

Despite the many studies cited above, experimental evidence of the mechanism of water invasion to dry pores under unstable conditions at the wetting front is still lacking. Specifically, the relationship between pore velocity and contact angle (Eq. (6)) was never tested in an actual porous media. Therefore, our objective was to visualize water movement through pores at the fingertip and demonstrate how the dynamic contact angle at unstable wetting fronts changed with pore water velocity. Two types of experiments were conducted. One looked at the wetting front advancement in all pores in an unstable finger. The second experiment focused on a single pore invasion. The results of the experiments are used to test the validity of the Hoffman relationship (Eq. (5)) to describe the pore-scale phenomena at an unstable wetting front of the fingertip.

## 2. Methods

The rapid displacement of fluids through pores at the wetting front was measured with a high-resolution, high-speed camera during the imbibition of water in air-dry sand. Three types of measurements were carried: At the tip of fingers moving down under gravity in 2-D and 3-D and at the single pore scale as water advances through it. A pressure transducer recorded matric potentials, and contact angles and velocities

were derived from image analysis.

### 2.1. Finger experiments in 2-D

The experimental setup for the finger experiment is shown in Fig. 1. The flow cell was constructed from glass. The glass was made hydrophobic by coating the surface with n-Octyltriethoxysilane (Gelest Inc. PA) via wet glass deposition. This coating delays the formation of a film along the cell wall, so the invasion of water in soil pores can be observed unimpeded. The flow cell dimensions were 30 \* 50 \* 1.6 mm, with the top open and a porous foam block at the bottom. The porous medium in the cells consisted of 20/30 grade quartz sand with grain size 0.6–0.8 mm (Unimin Corporation, Ottawa, MN) and had an average density of 1.56 gr/cm<sup>3</sup> in the cells. A 40 W LED lighting array (SP-E-365D LED Light, Genaray USA) behind the flow cell provided background lighting.

A differential pressure transducer (MPX5100DP piezoresistive transducer, NXP Semiconductors, Eindhoven, Netherlands) connected to an angled dispensing needle with an inner diameter of 0.41 mm (JENSEN GLOBAL, Santa Barbara, CA, USA) recorded the matric potential (Fig. 1). The tip was inserted at the back wall to minimize interference with the back lightning. Data were recorded at a frequency of 500 Hz via a DATAQ data acquisition kit (DI-1100 USB data acquisition starter kit, DATAQ INSTRUMENTS, Akron, Oh, USA).

A high-speed camera (Photron Fastcam S9 type 900K, Photron USA, Inc., CA) continuously visualized the pore liquid movement in a 25.6 mm by 25.6 mm area in the cell at 500 frames (1024×1024 pixels) per second at a spatial resolution of 25  $\mu\text{m}$  pixels. The camera's memory card stored 10,898 images before the recording was triggered. The recording frequency of 500 frames per second corresponded to 21.8 s of pore liquid movement. Stored images were transferred to a laptop at the

end of each recording as an AVI file. Photron FASTCAM Viewer 4 software (Photron USA, Inc., CA) was used to visualize the images.

Eleven experiments were performed. In each Run, water was applied at a rate of 15  $\mu\text{l}/\text{min}$  at the top of the cell through a dispensing needle with an inner diameter tip of 0.83 mm (JENSEN GLOBAL, Santa Barbara, CA, USA) with a syringe pump (KD Scientific Inc., Model 101). To enhance visualization, the water was dyed with 1 mg/L Brilliant Blue FCF (Warner-Jenkinson Co., Inc., Mo). Of the eleven experiments, two runs were selected where the pressure fluctuations were successfully acquired in conjunction with camera recordings before the wetting front advanced too far from the pressure sensor. These runs were labeled Run I and Run II.

The recording started for Run I 3.1 min after the start of the water application, while for Run II, water was applied for 4.3 min before the recording began. For both runs, the camera recording lasted 21.8 s. The tensiometer angled tip diameter was slightly smaller than the sand grains and was assumed to behave as another sand grain. A summary of Run I and Run II is provided in the Supplementary Materials Table S.1.

#### 2.1.1. Data analysis of 2-D finger experiments

The high-speed recordings of the infiltration Run I and II (the URLs provided in Appendix A) were analyzed frame-by-frame. The wetted area was cropped and saved as separate images. First, the red channel value of each pixel in the initial image was subtracted from the subsequent images using MATLAB Image Processing Toolbox (The MathWorks, Inc., Image Processing Toolbox version: 11.4, Release 2021b), resulting in zero values (Black) whenever the subsequent image pixels were identical to the initial image pixels. Pixels in subsequent images where the water advanced were no longer identical to the same pixel in the initial image and had non-zero red channel values, which were then

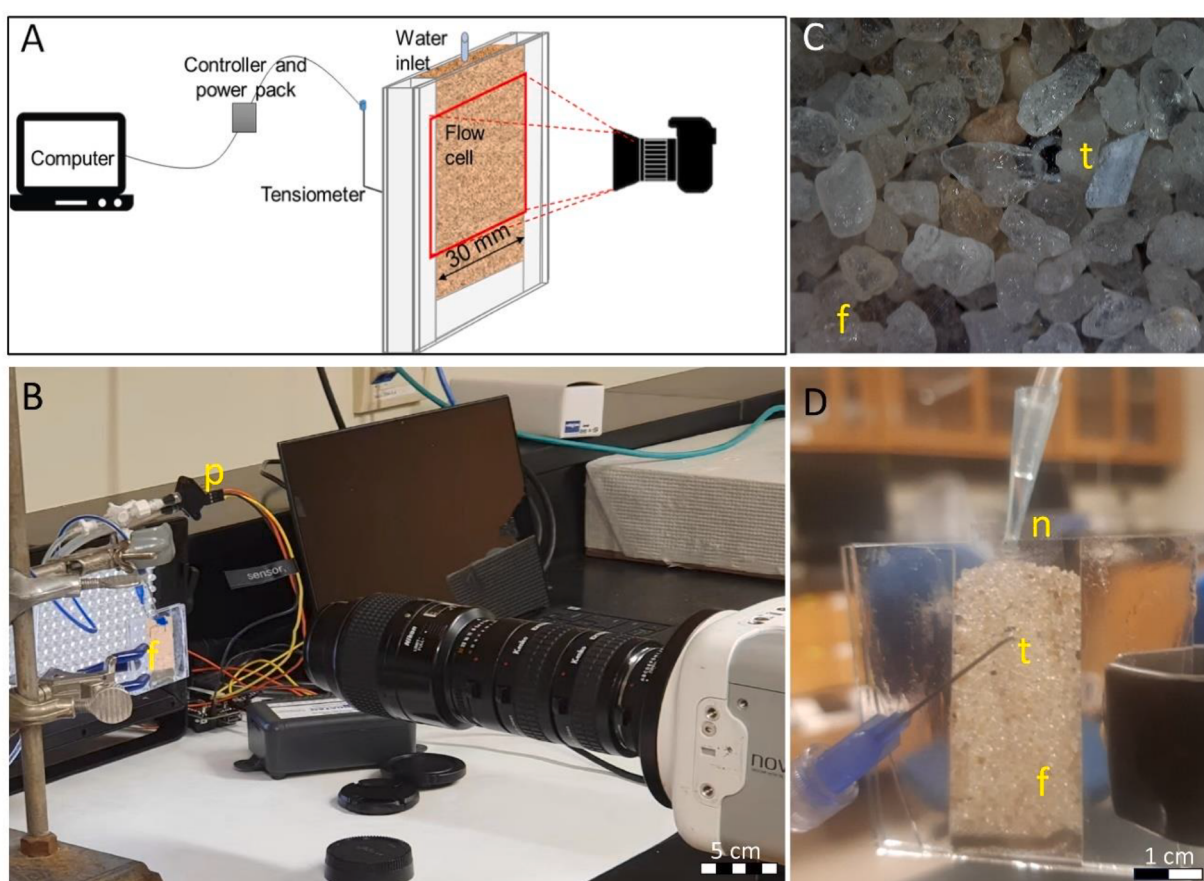


**Fig. 1.** (A) Schematic of the experimental setup; (B) photograph of the experiment with the sand in the flow cell (labeled f) and the pressure transducer for the tensiometer (labeled p); (C) closeup image of the sand in the cell (labeled f) and (D) the tip of the needle tensiometer (labeled t).

set to one. A matrix of zeros (black) and ones (white) was used for further analysis. The MATLAB code is available in Supplementary Materials, Section S.2. Variations due to changes in lighting and cell were filtered out with a MATLAB moving average filter of two values.

Water invasion through pores at the front was identified where the black pixels changed to white from one image to the next. The distance traveled was equal to the product of the pixel diameter and the number of pixels that changed value. The velocity was obtained by dividing the distance by the time between two consecutive frames (0.002 s apart). Although the time between frames is short, it limits the highest velocity that can be measured.

The matric potential or the negative water pressure at the wetting front at the fingertip was expressed in length units (i.e., energy per unit weight of water). Since the matric potential was measured at the tensiometer, an adjustment was necessary to obtain the matric potential at the fingertip. Assuming the hydraulic gradient was unity, the vertical distance between the tensiometer and the fingertip was added to the tensiometer reading.

## 2.2. Finger experiments in 3-D

Two additional 3-D experiment runs (Run III and IV) were performed to investigate whether hydrophobic silane-treated front and back walls altered the flow dynamics. Specifically, we examined whether the wetting front is discontinuous and water advances one pore at a time, which are the required conditions for deriving Eq. (5). The pore water velocity could not be measured because the water movement in 3-D is in all directions. The highspeed camera cannot estimate the direction; hence, the velocity cannot be calculated from the distance the meniscus moved between the consecutive frames.

For these 3-D experiments, a 4 mm thick layer of unwashed 20/30 sand (Unmin Corporation, Ottawa, MN), with grain size 0.6–0.8 mm, was packed in a transparent flow cell without a front plate that was 50 mm long and 18 mm wide. The cell was placed at a 30° angle, the steepest possible incline, without the sand spilling out. Water with 1 mg of brilliant blue/liter with a syringe pump (KD Scientific Inc., Model 101) that was applied at a 15  $\mu\text{l}/\text{min}$  rate formed the finger. The high-speed camera, a grayscale-sensitive Photron Nova S6-800, was placed above the cell, pointing down at a 60° angle. The cell and camera setup are presented in Fig. S.8.1. Background lighting consisted of a 40 W LED lighting array (SP-E-365D LED Light, Genaray USA). The resolution in Run III was 0.009 mm/pixel, and in Run IV, it was 0.0201 mm/pixel. During the experiment, the camera captured 21,821 images at 500 fps, resulting in a video length of 43.642 s. The camera resolution was 1024 by 1024 pixels. The image processing was similar to the 2-D experiments. Details are given in Supplemental Material S6

## 2.3. Pore-scale follow-up experiment

To analyze the pore-scale phenomena at the fingertip (Section 2.1.), the meniscus movement in a single pore was traced, and the contact angle was measured. The flow cell used in this follow-up experiment was a 6.5 mm x 2 mm x 33 mm n-Octyltriethoxysilane (Gelest Inc. PA) coated glass cell open at the top and closed with foam from the bottom. The cell was packed with dry sand with an average diameter of 1.5 mm. (Unmin Corporation, Ottawa, MN). This experiment was part of a colloid displacement study. The water was applied to the top of the cell using a syringe pump (ALA Scientific Instruments model NE-4000) at a constant flow rate of 10  $\mu\text{l}/\text{min}$  through an 18-gauge needle (inner diameter of 0.83 mm). The camera used in this experiment (Edgertronic SC2 high-speed camera, Edgertronic USA, Inc., CA) captured the wetting front movement at a resolution of 1280×864 pixels. A 2x lens (1-6010 Coupler, 1-6030 2X Adapter, 1-60135 Zoom body tube, 1-60112 Lens attachment, Navitar, Inc., USA) was used, resulting in a larger magnification over 1.72 by 1.16 mm viewing area with a resolution of 1.35  $\mu\text{m}$  per pixel. The URL link to the high-speed recording is provided in

## Appendix A.

The midpoint of the meniscus in each frame was tracked manually. The meniscus velocity was calculated by dividing the difference in midpoint location in the flow direction by the time between consecutive frames. A detailed explanation of this analysis and calculation procedure can be found in Supplementary Materials S.3. The upper and lower solid-water-air interface coordinates were recorded to calculate the dynamic contact angle. These coordinates were then used in the apex-contact line method (Ngan et al., 1982; 1989), simplified by Bian\_(2004) and previously used by Baver et al. (2014). A detailed explanation of contact angle calculation can be found in Supplementary Materials S.3.

## 3. Results

The results consist of three parts: First, the characteristics of the pore water movement in the 21.8 s high-speed recordings of Run I and Run II are presented (Section 3.1), followed by a detailed description of one pore invasion event. Finally, the results of the pore scale follow-up experiment are given in Section 3.3.

### 3.1. Finger experiment

The two selected runs were labeled Run I and Run II. The recording of Run I started after 3.1 min (190 s), and for Run II, after 4.3 min (258 s) of water was applied, it lasted 21.8 s. The URLs of the high-speed digital footage of Run I and Run II are found in Appendix A.

#### 3.1.1. Two-dimensional pore water movement characteristics in Run I and Run II

The high-speed recordings (URL links are listed in Appendix A) show the water movement at the wetting front at the fingertip. While the water application was steady and continuous, the finger advancement was intermittent, localized, and sporadic. In the recording for Run I, the front was stationary for 15 s, and during the remaining 6.8 s, 20 pore invasions occurred with maximum velocities ranging from 33 to 255 mm/s. For Run II, 26 events occurred in 4.11 s with maximum speeds of 16 to 215 mm/s. Almost all pore invasions occurred at the fingertip. In Run I, pore invasions were first downward and then sideways after the downward movement was halted just above some large pore spaces (shown as white in Fig. 2) and only downwards in Run II. An example of a before and after image of a fast pore invasion and filling of the pore space is shown in Fig. 2. The sand particles are brown; the white areas are air-filled spaces between the grains; the blue is the infiltrated water in the finger. Fig. 2A is the image of Run I just before the pore invasion, around 18 s after the start of the recording, and Fig. 2B is 0.24 s later, with the area invaded sideways at the left of the front and circled in yellow. A similar sequence before and after is shown for Run II in Fig. 2C and D of a downward pore invasion taken 13 s into the Run with 0.21 s between the two images. Additional images of pore invasion events (and pore cavity filling afterward) are summarized in Fig. S4.1 and S4.2 in Supplementary Materials S.4.

The velocity of the water during the pore invasion and filling event in Fig. 2 is not constant, as seen for the entire 21.8 s recording for Runs I and II in Fig. 3. Each event starts with a high velocity (ranging from 70 up to  $2.5 \times 10^3$  mm/s) through the pore neck and lower velocities (negative and positive) when the pore cavity fills. Another high velocity can be seen during an event when an additional pore is invaded (Fig. 3). Backflows caused negative velocities due to the redistribution of water within the finger. The velocity in a single pore is further discussed in Section 3.1.2. The velocities during pore breakthrough were faster by orders of magnitude from the water application flux (0.46 mm/s) and the saturated hydraulic conductivity (2.5 mm/s or average velocity of 7.1 mm/s, based on the 20/30 sand saturation moisture content of 0.35, measured by DiCarlo (2007)).

Matric potential per unit weight (i.e., length units) over time for Run I and Run II are presented in Fig. 4. The time axis is the same as in Fig. 3.

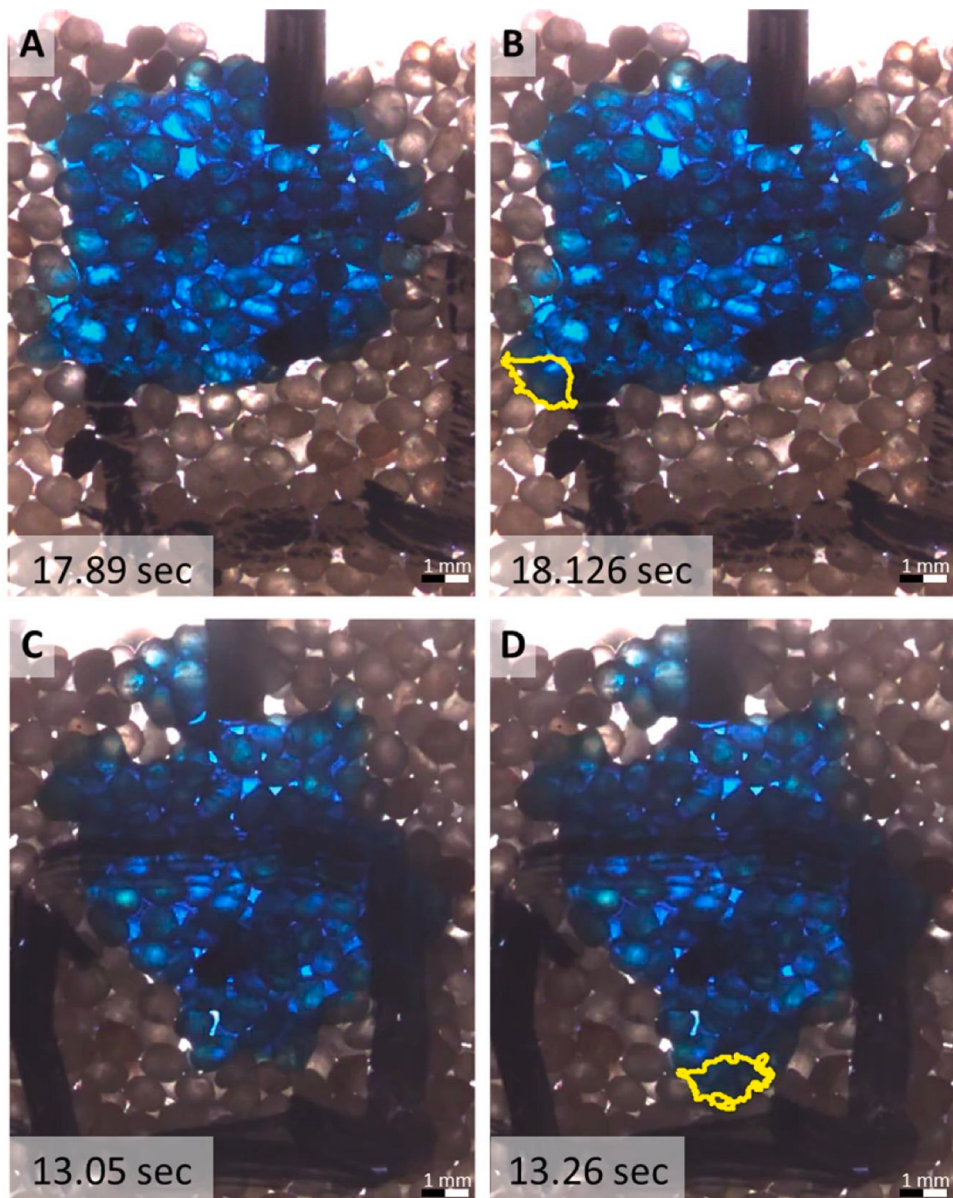


**Fig. 2.** Images of 10.05 by 12.61 mm of (A-B) one pore invasion event taken from Run I and (C-D) one from Run II. Images A and C are from just before the invasion events, and B and D are at the end of the events. The yellow-enclosed areas contain the pores between the sand grains just invaded by the blue-dyed water. The time each image was taken is indicated in its lower left-hand corner.

After the wetting front reached the pressure sensor, the matric potential increased from around -8 cm to between -3 and -4 cm in both runs. The matric potential at the tensiometer decreases when the fingertip is further down in accordance with the theory (Selker et al., 1992b) and other finger flow experiments (e.g., DiCarlo 2007). Within this general trend, the matric potential decreased by 3 mm after the water invaded a pore and then increased slowly until the next pore invasion event. These changes are illustrated in the small subplots in Fig. 4A and B.

The matric potential decreased faster in Run II, where the breakthrough was downward than in Run I, where water also moved laterally (Fig. 4). The decrease in matric potential is directly related to the vertical distance above the wetting front (Geiger and Durnford, 2000). So, if the front advances downward faster in Run II than in Run I, the matric potential will also decrease faster in Run II.

### 3.1.2. Velocities and matric potential for a single event in the 2-D finger experiment

In the previous section, we gave the results of the entire 21.8 s

recording. A detailed example of a pore invasion and pore cavity filling at the fingertip is shown in Fig. 5 to illustrate these processes better. The events selected are around 18 s after the start of the recording. Letters a-f in Fig. 5A correspond to the images in Fig. 5B. This invasion event lasted 0.24 s, with water advancing 0.917 mm at an average velocity of 3.9 mm/s. However, the movement mainly occurred in short bursts with a maximum velocity of 138 mm/s (Fig. S5 in the Supplementary Materials). Four stages were observed. In the first stage, water moved slowly a short distance into the pore as a film (Fig. 5B, a,b). Then, the movement changed to a fast flow through the pore, where the meniscus moved 0.6 mm in less than 0.03 s (Fig. 5B, b-c). In the second stage, the water moved slower between points d and e in Fig. 5B. The third stage (Fig. 5B, e, f) was characterized by the film completing the grain coating. The wetting front remained stationary in the fourth stage, with only tiny advancements and some oscillating. Additional detailed examples of pore invasion and filling of the space below are shown in Supplementary Materials S.6. In Fig. S6, it is shown that a water film formed first, and immediately afterward, the breakthrough occurred. While the water fills

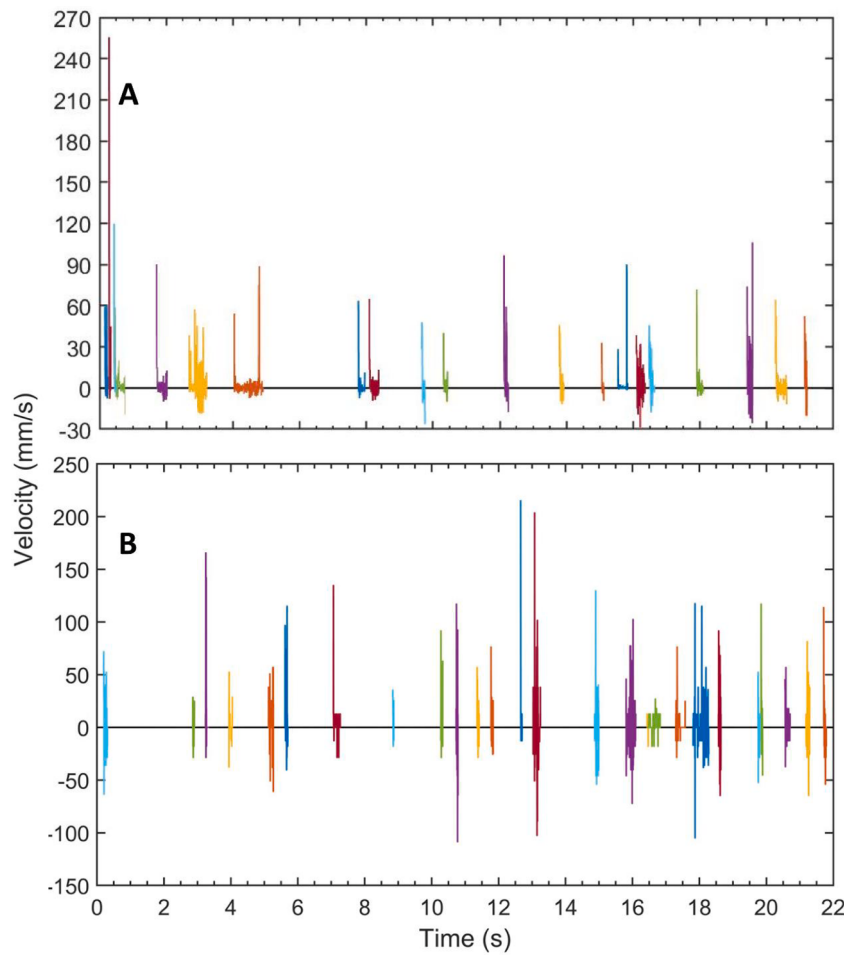


**Fig. 3.** Velocities in pores during pore invasions for (A) Run I and (B) Run II. Different colors are used to differentiate between pore invasions that are close together. The x-axis represents the time from the start of the recording by the high-speed camera.

the pore presented in Fig. S6, water is simultaneously released from a pore further above (Fig. S7).

### 3.1.3. Analysis of Run I and II

In Run I, when the advancing wetting front reached the large pores (as indicated by the white spots), the water in the pores moved laterally, while in the entire Run II, the main flow direction was downward, indicating that water tends to move through the smaller pores (Figs. 2A and S4.1). To explain this phenomenon for unstable wetting fronts, we note that Rusanov et al. (2019) and Tokunaga and Wan (2001) indicate that a contact film (also called precursor film) forms in a dry fracture when the contact angle is close to  $90^\circ$ . This contact film will allow the downward movement of water through the pore. In addition, we pose that the breakthrough is through the smallest pore near the wetting front. Macroscopically, the meniscus curvature in all pores is the same and less at the bottom of the column than higher up in the finger. Adding a drop of water with a fully developed capillary fringe in a small pore will increase the contact angle to a greater extent than in a larger pore. Hence, the critical contact angle to form a film will be attained first in the smallest pore. Once a film forms, the water can move through the pore. In previous studies (Wallach et al., 2013), this phenomenon has been called "partial wettability". Indeed, the soil acts as hydrophobic, and once a water film exists, the grains around the pore behave as hydrophilic for a short moment.

The expansion almost always occurs near the fingertip - on average, less than 0.6 mm - and not higher up in the finger. We can explain this using a Young-Laplace formulation to describe the connection between the matric potential and contact angle at the wetting front,

$$h = -\frac{2\gamma}{R} \quad (6a)$$

where  $h$  is matric potential (in units of pressure), and  $R$  is the radius of the meniscus curvature, which for flow in the pores can be assumed as:

$$R = \frac{r}{\cos\theta_d} \quad (7)$$

where  $r$  is the pore radius. The matric potential decreases with the distance above the fingertip. The radius of the meniscus at the fingertip is thus the greatest. Assuming that whenever water is added, all menisci expand similarly, the critical contact angle for advancement of around  $90^\circ$  is first exceeded at the fingertip. Note that the 3-D experiment at a  $30^\circ$  inclination presented next in Section 3.2 (and in Supplementary Materials S8) gives some credence to this explanation. Further investigations are needed to confirm the phenomena.

### 3.2. Three-dimensional finger experiment

The individual 3-D pore invasion events for Run III (Fig. S.8.2) and Run IV (Fig. S.8.3) show many similarities and some differences with the 2-D pore invasions (Figs. 2, S4.1, S4). Similar was that the pore invasions were intermittent. In both dimensions, water rushed through and filled one or several pores, followed by a period without apparent water movement. Despite the similar physics, the duration of the pore infiltration events of Run I was significantly greater than the other Runs II, III, and IV, which were not significantly different (Fig. 6). Run I was

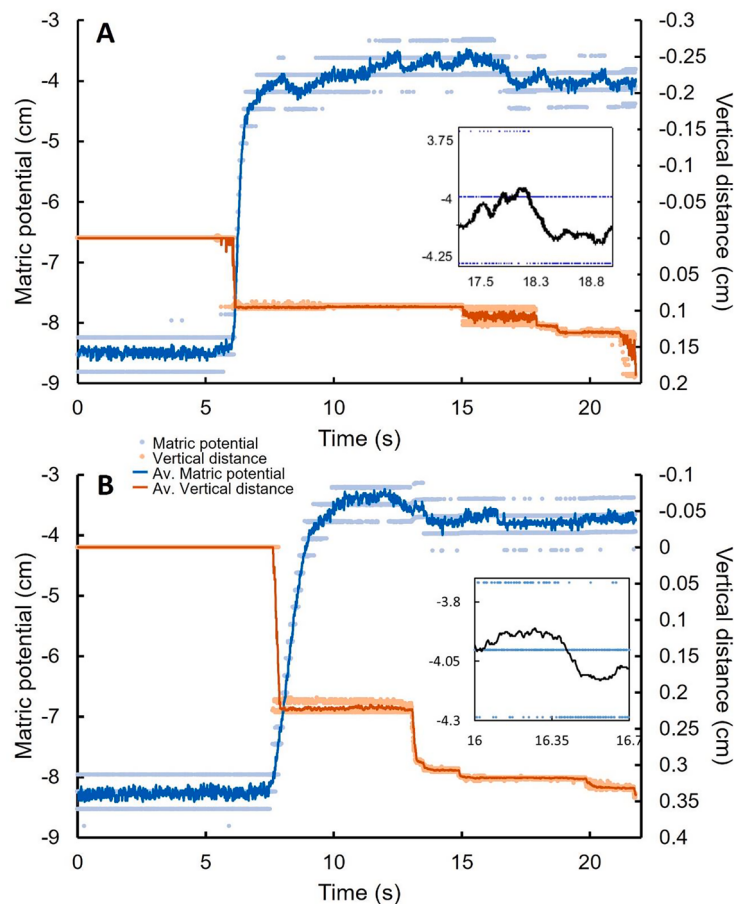


**Fig. 4.** The overall matric potential readings during Run I (A) and Run II (B). Light blue dots represent actual recorded data corrected to the wetting front height. The blue line represents moving averages for the height-adjusted data. The orange dots and the orange line represent the measured and moving average of the vertical distance between the front and the sensor. The subplot in Figure A relates to Fig. 5A, B and in Figure B to Figs. S7 and S8 in the supplementary material.

different because there was a large gap between the sand grains under the finger-wetting front (Figs. 2A, B, S4.1), forcing the water to move sideways. In Run II, the fingertip did not encounter a gap (Figs. 2C, D and S4.2), and the pore invasions were generally downwards. In 3-D, it is easier for the water to flow around gaps; hence, irregular packing does not affect the flow direction. Thus, although the finger width might differ in 2-D and 3-D, the advance of the wetting front through intermittent invasions of pores is similar.

Another difference was that the pore invasion in 2-D was in a much narrower band close to the finger-wetting front Figs. 2, S4.1, S4.2 than in 3-D experiments (Fig. S8.2, S8.3). The reason is that the 3-D cells were at a 30° slope and the 2D cells vertical. Thus, the effect of gravity was half in 3-D than that in 2-D. Since matric potential and gravity are related (Selker et al., 1992b), the matric potential decreases more slowly in 3D behind the fingertip than in 2D. Matric potential and likelihood of pore invasion are correlated, hence the wider band of pore invasion when gravity is reduced, such as in the 3-D experiments. A more detailed explanation is given in Supplementary Material S8 and the discussion. Thus, although there are some differences between the 2-D and 3-D experiments (requiring further study), the 3-D experiments show distinctly that the intermittent nature of the pore invasion events in 2-D did not depend on the Silane coating of the walls.

### 3.3. Pore-scale follow-up experiment

This follow-up experiment tracked water movement through a single pore (Fig. 7A). To find the pore water velocity, the midpoint of the meniscus was tracked. The dynamic contact angle was calculated based

on the recorded coordinates of the upper and lower solid-water-air interfaces.

The pore invasion occurred during 17 frames of 0.002 s each. In the first nine frames, the meniscus was unobservable because, in the first eight frames, the meniscus was not within the focal plane. During the ninth frame, the image was blurred because the velocity was so high that even the high-speed camera in 0.002 s could not capture the movement. Frame 10 is the first image where the meniscus is clearly visible and is shown in Fig. 7A. The velocity rapidly decreased from 27 cm/s (2300 m/d) (Fig. 7B) in frame 10, and the front was stationary in frame 17. The meniscus moved backward as invasion occurred at other portions of the cell.

The dynamic contact angles ranged from 52° in frame 10 when the meniscus velocity was highest to 28° when the front was stationary. Higher velocities were correlated with larger contact angles (Fig. 7B, Table S2 in the Supplementary Materials). The dashed line in Fig. 7B represents the Hoffman-Bauer model (Eq. (5)) with a static contact angle of 32°. The 32° contact angle agreed with that by Aminzadeh et al. (2011) for similar sands. The measured dynamic contact angles and velocity relationship generally agreed with the Hofmann-Bauer model with an  $R^2 = 0.63$  and MSE of 0.002 radians.

After the ten frames shown in Fig. 7C, the meniscus receded. Due to the hysteretic effects of the contact line, the contact angle was less than the static contact angle (Drelich, 2019) and ranged from 12 to 22°. For these conditions, the Hoffman-Bauer relationship was not valid for calculating the contact angles.

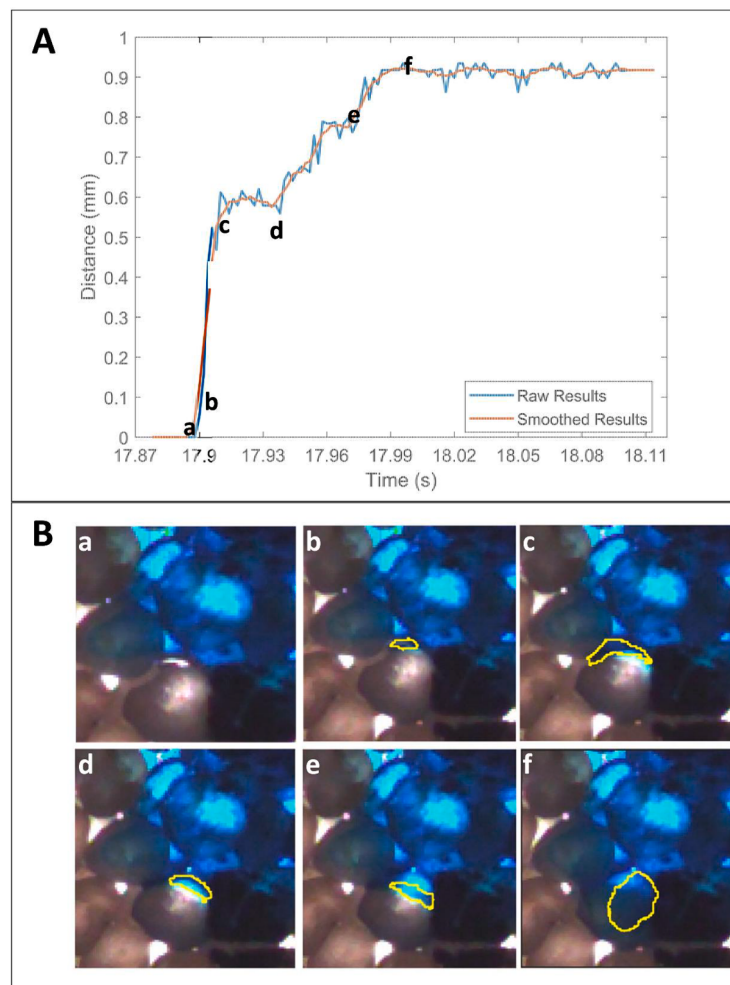


**Fig. 5.** (A) Details of the travel distance of water in a single pore at the wetting front for Run I. The blue line refers to the observed distance traveled by the water in the pore at the wetting front during the invasion. The orange line is the smoothed data. Letters a-f refer to the wetting front advancement stage corresponding to each Figure a-f in Fig. 5B. (B) Still, captions from Run I. Figures show the advance of the water at the wetting front through a single pore (a) before invasion starts, (b) when the film enters the pore, (c) when the water rapidly advances through the pore, (d) filling of the pore cavity and (e-f) spreading. The figure letters correspond to those in Fig. 5A.

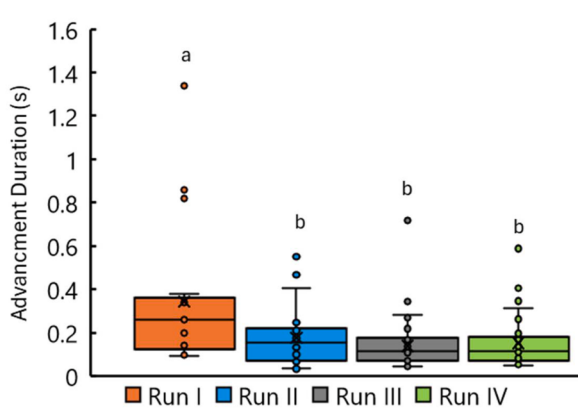


**Fig. 6.** Box plot of the duration of the individual pore water invasion events of Runs I-IV. Letters above the Runs mark significant differences. For all Runs with the same letter, the difference between the means is not statistically significant. If two runs have different letters, they are significantly different.

#### 4. Discussion and conclusion

##### 4.1. Interpretations of findings

A high-speed camera and a tensiometer were used in a small glass chamber to observe the pore invasions and matric potential in dry, coarse sand. The chamber was thin to allow for visualization of the pore water movement. The water at the wetting front always moved between the sand grains without touching the highly hydrophobic silane-coated glass wall. While the cell width and wall effect may affect the invasion velocities (and contact angles), the discrete dynamics of the single pore invasions are a result of the porous media characteristics and not a boundary effect. This was corroborated in additional experimental runs conducted in a wider cell without a front wall, presented in Section S.8 of the Supplementary Materials.

Water applied on dry, coarse sand at rates less than saturated conductivity generates unstable wetting fronts. The potential across the finger boundary with the dry soil is discontinuous. When the water reached the tensiometer, the matric potential increased suddenly, giving credence to the assumption that the matric potential across the wetting front is discontinuous. Moreover, unlike the typical Darcy flow assumption, in which water movement is averaged over several pores, we found that the water advanced through each pore at different times

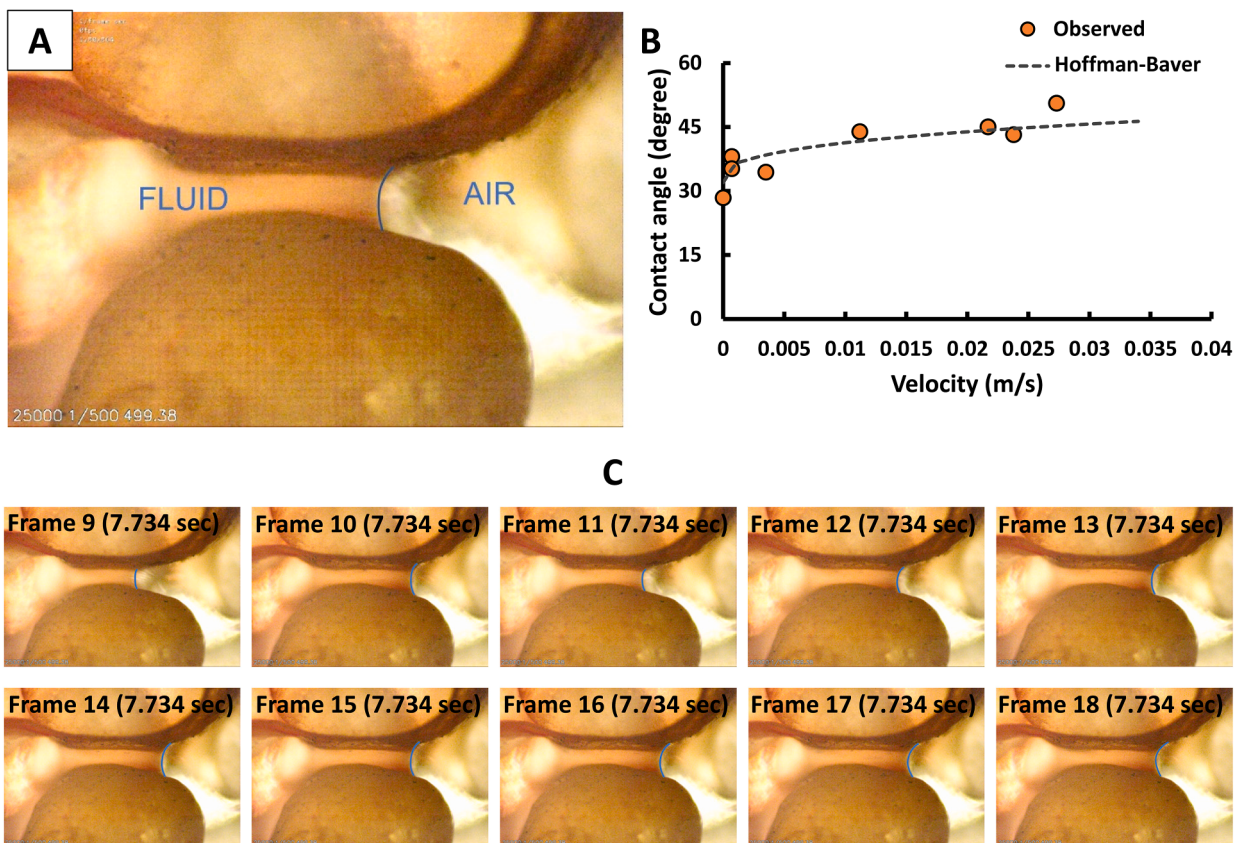


**Fig. 7.** (A) Image captured from the pore scale experiment at 5.742 seconds. The interface and the two fluid phases are highlighted in blue. The flow direction in the pore is from left to right. (B) observed (orange circles) and predicted (dashed line) relations between velocity (x-axis) and dynamic contact angle (y-axis). (C) image series of the advancing contact angle. The first image is blurry, and the contact angle was impossible to calculate because of the high velocity. The last image is from the beginning of the pin-back interface stage, and the receding contact angle did not match the Hoffman-Baver equation.

in what appeared to be hydraulic jumps with several distinct phases. First, a partial film forms on the grain (Figs. 5B b and S6b in the Supplementary Materials). Next, the water flows through the pore at high velocity (Figs. 5B b-f and S6 c-e). Then, the velocity decreases while filling the void below the invaded pore (Figs. 5B g-h and S6 f-h in the Supplementary Materials). The maximum speed was 25.5 cm/s (Fig. 3). We also observed that the dynamic contact angles were larger at high velocities than at lower speeds (Fig. 7). It followed the Hoffman-Baver relationship between contact angle and porewater velocity based on the Hoffman (1975) experiment.

#### 4.2. Comparison of a compact and unstable wetting front

The matric potential is continuous across a compact infiltration front (i.e., piston flow) and increases monotonically above the front (i.e., becomes less negative). Since the water content and matric potential are related according to the water retention curve, the water content increases with the vertical distance above the wetting front. Hence, the compact imbibition front is diffuse.

On the other hand, for unstable wetting fronts, the matric potential across the front is discontinuous. Unlike the stable front, the matric potential increases with depth and is the greatest at the wetting front. Under these conditions, films form only when the matric potential is near zero (Rusanov et al., 2019; Tokunaga and Wan, 2001); thus, water must accumulate, and pressure must build up before the water can enter the smallest pore. The zero matric potential implies that the meniscus radius is infinite (i.e., a flat meniscus). The smallest amount of water is needed in the smallest pore at the fingertip for the meniscus to become flat. Breakthrough will, therefore, also occur through the smallest pores as is the case for the "stable front", but with the difference that the water

moves through only one pore at a time intermittently filling up few large pores behind the new front.

The selection of the "smallest pore" for breakthrough also explains the extreme sensitivity of the fingered flow chamber experiment results to packing. When the chamber is not packed at once, it results in the layering of fine and coarse layers because each time sand is poured into the chamber, it is sorted by gravity. A coarse layer will hold up the downward movement and promote lateral flow. It is similar to our Run I; when the wetting front reached a large pore, it moved sideways. Therefore, non-homogenous packing results in varying finger thickness, as shown, for example, by Wallach and Jortzick (2008). On the other hand, evenly thick fingers with uniform pore sizes were observed in well-packed sand (Glass et al., 1989). Also, in our earlier experiments in the 1990s (not published), we could direct the direction of the fingers by filling in the chamber. A sand pile in the center resulted in fingers close to the side walls of the chamber, and two heaps at the sides directed the fingers to the center of the chamber.

In conclusion, this experimental study implies that theoretical and modeling approaches that assume that the matric potential across the front is discontinuous are most promising to advance the theory of unstable wetting fronts. However, this study was limited to wetting front behavior in homogeneous sandy soils. Further studies are needed to study the effect of non-homogenous soils, water repellency and the role of gravity.

#### CRediT authorship contribution statement

**Naaran Brindt:** Writing – review & editing, Writing – original draft, Methodology, Investigation, Conceptualization. **Xinying Min:** Methodology, Investigation. **Jiuzhou Yan:** Investigation. **Sunghwan Jung:**

Writing – review & editing, Supervision, Resources, Methodology. **J-Yves Parlange:** Writing – review & editing, Supervision, Conceptualization. **Tammo S. Steenhuis:** Writing – review & editing, Writing – original draft, Supervision, Methodology, Conceptualization.

## Declaration of competing interest

The authors declare that they have no known competing financial interests or personal relationships that could have appeared to influence the work reported in this paper.

## Data availability

Data will be made available on request.

## Supplementary materials

Supplementary material associated with this article can be found in the online version at [doi:10.1016/j.advwatres.2024.104661](https://doi.org/10.1016/j.advwatres.2024.104661).

## Appendix A

### URL links to video files

The highspeed videos of Run I, Run II, and the pore scale supplemental run can be viewed at the URL 10.7298/gtdr-0032. The highspeed videos of Run III and Run IV can be viewed at the URL <https://hdl.handle.net/1813/114207>

These files are compressed high-speed video recordings of the unstable infiltration runs to dry sand packed into vertical, n-Octyl-triethoxysilane-coated flow cell for Run I, Run II, and the pore scale supplemental run, and a 30°, open front flow cells for Runs III and IV. The compression standard used was H.264. Video files were recorded at 500 fps and played at 30 fps. More data about the video files is presented in the supplied links above, the Readme files within, and in Supplementary Material S1 and S8.

## References

- Aker, E., Måløy, K.J., Hansen, A., Basak, S., 2000. Burst dynamics during drainage displacements in porous media: simulations and experiments. *EPL Europhys. Lett.* 51 (1), 55–61. <https://doi.org/10.1209/epl/i2000-00331-2>.
- Aminzadeh, B., DiCarlo, D.A., Wallach, R., 2011. The effect of contact angle on saturation overshoot. *Vadose Zone J.* 10 (1), 466–468. <https://doi.org/10.2136/vzj2010.0047>.
- Andreini, M.S., Steenhuis, T.S., 1990. Preferential paths of flow under conventional and conservation tillage. *Geoderma* 46 (1–3), 85–102. [https://doi.org/10.1016/0016-7061\(90\)90009-X](https://doi.org/10.1016/0016-7061(90)90009-X).
- Aslam, R.A., Shrestha, S., Pandey, V.P., 2018. Groundwater vulnerability to climate change: a review of the assessment methodology. *Sci. Total Environ.* 612, 853–875. <https://doi.org/10.1016/j.scitotenv.2017.08.237>.
- Armstrong, R.T., Evseev, N., Koroteev, D., Berg, S., 2015. Modeling the velocity field during Haines jumps in porous media. *Adv. Water Resour.* 77, 57–68. <https://doi.org/10.1016/j.advwatres.2015.01.008>.
- Bakhshian, S., Rabban, H.S., Shokri, N., 2021. Physics-driven investigation of wettability effects on two-phase flow in natural porous media: recent advances, new insights, and future perspectives. *Transp. Porous Media* 140, 85–106. <https://doi.org/10.1007/s11242-021-01597-z>.
- Bauer, C.E., Parlange, J.Y., Stoff, C.R., DiCarlo, D.A., Wallach, R., Durnford, D.S., Steenhuis, T.S., 2014. Capillary pressure overshoot for unstable wetting fronts is explained by Hoffman's velocity-dependent contact-angle relationship. *Water Resour. Res.* 50 (6), 5290–5297. <https://doi.org/10.1002/2013WR014766>.
- Beatty, S.M., Smith, J.E., 2013. Dynamic soil water repellency and infiltration in post-wildfire soils. *Geoderma* 192 (1), 160–172. <https://doi.org/10.1016/j.geoderma.2012.08.012>.
- Berg, S., Ott, H., Klapp, A., Stempsoni, M., 2013. Real-time 3D imaging of Haines jumps in porous media flow. *Proc. Natl. Acad. Sci.* 110 (10), 3755–3759. <https://doi.org/10.1073/pnas.1221373110>.
- Bian, X., 2004. Liquid slug motion in an oscillatory capillary tube (PhD thesis). The University of Michigan. <https://hdl.handle.net/2027.42/124019>. Accessed Feb 25, 2024.
- Bouchard, D.J., Chandra, S., 2020. Infiltration of impacting droplets into porous substrates. *Exp. Fluids* 61 (11), 235. <https://doi.org/10.1007/s00348-020-03056-9>.
- Brindt, N., Wallach, R., 2017. The moving-boundary approach for modeling gravity-driven stable and unstable flow in soils. *Water Resour. Res.* 53 (1), 344–360. <https://doi.org/10.1002/2016WR019252>.
- Brindt, N., Wallach, R., 2020. The moving-boundary approach for modeling 2-D gravity-driven stable and unstable flow in partially wettable soils. *Water Resour. Res.* 56 (5) <https://doi.org/10.1029/2019WR025772>.
- Brindt, N., Parlange, J.Y., Steenhuis, T.S., 2023. Unstable preferential flow in porous media. Goss, M.J., Oliver, M., Eds. *Encyclopedia of Soils in the Environment*, 2nd ed. Academic Press, pp. 314–320. <https://doi.org/10.1016/B978-0-12-822974-3.00160-9>.
- Cuesta, C., van Duijn, C.J., Hulshof, J., 2000. Infiltration in porous media with dynamic capillary pressure: travelling waves. *Eur. J. Appl. Math.* 11 (4), 381–397. <https://doi.org/10.1017/S0956792599004210>.
- Cueto-Felgueroso, L., Juanes, R., 2008. Nonlocal interface dynamics and pattern formation gravity-driven unsaturated flow through porous media. *Phys. Rev. Lett.* 101 (24) <https://doi.org/10.1103/PhysRevLett.101.244504>, 244504–1.
- DiCarlo, D.A., 2004. Experimental measurements of saturation overshoot on infiltration. *Water Resour. Res.* 40 (4), 1–10. <https://doi.org/10.1029/2003WR002670>.
- DiCarlo, D.A., 2007. Capillary pressure overshoot as a function of imbibition flux and initial water content. *Water Resour. Res.* 43 (8), 1–7. <https://doi.org/10.1029/2006WR005550>.
- Drelich, J., 2019. Contact angles: from past mistakes to new developments through liquid-solid adhesion measurements. *Adv. Colloid Interface Sci.* 267, 1–14. <https://doi.org/10.1016/j.cis.2019.02.002>.
- Egorov, A.G., Dautov, R.Z., Nieber, J.L., Sheshukov, A.Y., 2003. Stability analysis of gravity-driven infiltrating flow. *Water Resour. Res.* 39 (9), 1–14. <https://doi.org/10.1029/2002WR001886>.
- Eliassi, M., Glass, R.J., 2003. On the porous continuum-scale modeling of gravity-driven fingers in unsaturated materials: numerical solution of a hypodiffusive governing equation that incorporates a hold-back-pile-up effect. *Water Resour. Res.* 39 (6), 1–14. <https://doi.org/10.1029/2002WR001535>.
- Esfandyari, H., Haghhighi Hoseini, A., Shadizadeh, S.R., Davarpanah, A., 2021. Simultaneous evaluation of capillary pressure and wettability alteration based on the USBM and imbibition tests on carbonate minerals. *J. Pet. Sci. Eng.* 200, 108285 <https://doi.org/10.1016/j.petrol.2020.108285>. HYPERLINK.
- Gardner, W.R., Mayhugh, M.S., 1958. Solutions and tests of the diffusion equation for the movement of water in soil. *Soil Sci. Soc. Am. J.* 22 (3), 197–201. <https://doi.org/10.2136/sssaj1958.03615995002200030003x>.
- Geiger, S.L., Durnford, D.S., 2000. Infiltration in homogeneous sands and a mechanistic model of unstable flow. *Soil Sci. Soc. Am. J.* 64 (2), 460–469. <https://www.crops.org/publications/sssaj/abstracts/64/2/460>.
- Glass, R.J., Yarrington, L., 2003. Mechanistic modeling of fingering, nonmonotonicity, fragmentation, and pulsation within gravity/buoyant destabilized two-phase/unsaturated flow. *Water Resour. Res.* 39 (3) <https://doi.org/10.1029/2002WR001542>.
- Glass, R.J., Steenhuis, T.S., Parlange, J.Y., 1989. Wetting front instability: 2. Experimental determination of relationships between system parameters and two-dimensional unstable flow field behavior in initially dry porous media. *Water Resour. Res.* 25 (6), 1195–1207. <https://doi.org/10.1029/WR025i006p01195>.
- Green, W.H., Ampt, G.A., 1911. Studies on soil physics, 1: the flow of air and water through soils. *J. Agric. Sci.* 4, 1–24. <https://doi.org/10.1017/S0021859600001441>.
- Hill, D.E., Parlange, J.Y., 1972. Wetting front instability in layered soils. *Soil Sci. Soc. Am. J.* 36 (5), 697–702. <https://doi.org/10.2136/sssaj1972.03615995003600050010x>.
- Haines, W.B., 1928. Capillary properties of moist granular media. *Nature* 122 (3077), 607–608. <https://doi.org/10.1038/122607a0>.
- Hilpert, M., 2012. Velocity-dependent capillary pressure in theory for variably-saturated liquid infiltration into porous media. *Geophys. Res. Lett.* 39 (6), L06402. <https://doi.org/10.1029/2012GL051114>.
- Hoffman, R.L., 1975. A study of the advancing interface. I. Interface shape in liquid—Gas systems. *J. Colloid Interface Sci.* 50 (2), 228–241. [https://doi.org/10.1016/0021-9797\(75\)90225-8](https://doi.org/10.1016/0021-9797(75)90225-8).
- Jarvis, N., Etana, A., Stagnitti, F., 2008. Water repellency, near-saturated infiltration and preferential solute transport in a macroporous clay soil. *Geoderma* 143 (3), 223–230. <https://doi.org/10.1016/j.geoderma.2007.11.015>.
- Jiang, T., Soo-Gun, O., Lattery, J.C., 1979. Correlation for dynamic contact angle. *J. Colloid Interface Sci.* 69 (1), 74–77. [https://doi.org/10.1016/0021-9797\(79\)90081-X](https://doi.org/10.1016/0021-9797(79)90081-X).
- Kim, M., Kim, K.Y., Lim, J.H., Kim, C.Y., Kim, S.G., Han, G., Han, W.S., Park, E., 2022. Pore-scale investigation of dynamic immiscible displacement in layered media using synchrotron X-ray micromotography. *Environ. Sci. Technol.* 56 (1), 282–292. <https://doi.org/10.1021/acs.est.1c05557>.
- Kim, S., Fezzaa, K., An, J., Sun, T., Jung, S., 2017. Capillary spreading of contact line over a sinking sphere. *Appl. Phys. Lett.* 111, 134102 <https://doi.org/10.1063/1.4991361>.
- Klute, A., 1952. Some theoretical aspects of the flow of water in unsaturated soils. *Soil Sci. Soc. Am. J.* 16, 144–148. <https://doi.org/10.2136/sssaj1952.03615995001600020008x>. Proc.
- Kmec, J., Fürst, T., Vodák, R., Šíř, M., 2019. A semi-continuum model of saturation overshoot in one dimensional unsaturated porous media flow. *Sci. Rep.* 9 (1), 1–12. <https://doi.org/10.1038/s41598-019-44831-x>.
- Kmec, J., Fürst, T., Vodák, R., Šíř, M., 2021. A two dimensional semi-continuum model to explain wetting front instability in porous media. *Sci. Rep.* 11 (1), 3223. <https://doi.org/10.1038/s41598-021-82317-x>.

- Lawes, J.B., Gilbert, J.H., Warington, R., 1882. On the Amount and Composition of the Rain and Drainage-Waters Collected at Rothamsted. William Clowes and Sons, London, U.K.
- Li, S., Liu, H., Wu, R., Cai, J., Xi, G., Jiang, F., 2022. Prediction of spontaneous imbibition with gravity in porous media micromodels. *J. Fluid Mech.* 952, A9. <https://doi.org/10.1017/jfm.2022.890>.
- McHale, G., Newton, M.I., Shirtcliffe, N.J., 2009. Dynamic wetting and spreading and the role of topography. *J. Phys. Condens. Matter* 21 (46), 4122. <https://doi.org/10.1088/0953-8984/21/46/464122>.
- Mielniczuk, B., Hueckel, T., 2022. Capillary water in 2-D drying-cracking soil sub-grain models: morphology and kinematics of evaporation and haines jumps. *Water Resour. Res.* 58, e2022WR031938 <https://doi.org/10.1029/2022WR031938>.
- Miyata, S., Kosugi, chirou, Nishi, Y., Gomi, T., Sidle, R.C., Mizuyama, T., 2010. Spatial pattern of infiltration rate and its effect on hydrological processes in a small headwater catchment. *Hydrological Processes* 24, 535–549. <https://doi.org/10.1002/hyp.7549>.
- Moebius, F., Or, D., 2012. Interfacial jumps and pressure bursts during fluid displacement in interacting irregular capillaries. *J. Colloid Interface Sci.* 377 (1), 406–415. <https://doi.org/10.1016/j.jcis.2012.03.070>.
- Morbidelli, R., Corradini, C., Saltalippi, C., Flammini, A., Dari, J., Govindaraju, R.S., 2018. Rainfall infiltration modeling: a review. *Water* 10 (12), 1873. <https://doi.org/10.3390/w10121873>.
- Ngan, C.G., Dussan, V., E, B., 1982. On the nature of the dynamic contact angle: an experimental study. *J. Fluid Mech.* 118, 27–40. <https://doi.org/10.1017/S0022112082000949>.
- Ngan, C.G., Dussan, V., E, B., 1989. On the dynamics of liquid spreading on solid surfaces. *J. Fluid Mech.* 209, 191–226. <https://doi.org/10.1017/S0022112089003071>.
- Nieber, J.L., Dautov, R.Z., Egorov, A.G., Sheshukov, A.Y., 2005. Dynamic capillary pressure mechanism for instability in gravity-driven flows; review and extension to very dry conditions. *Upscaling Multiphase Flow in Porous Media*. Springer-Verlag, pp. 147–172. [https://doi.org/10.1007/1-4020-3604-3\\_8](https://doi.org/10.1007/1-4020-3604-3_8).
- Nimmo, J.R., 2021. The processes of preferential flow in the unsaturated zone. *Soil Sci. Soc. Am. J.* 85 (1), 1–27. <https://doi.org/10.1002/saj2.20143>.
- Nissan, A., Wang, Q., Wallach, R., 2016. Kinetics of gravity-driven slug flow in partially wettable capillaries of varying cross section. *Water Resour. Res.* 52, 613–615. <https://doi.org/10.1002/2016WR018849>.
- Parlange, J.Y., Hill, D.E., 1976. Theoretical analysis of wetting front instability in soils. *Soil Sci.* 122 (4), 236–239. <https://doi.org/10.1097/00010694-197610000-00008>.
- Parlange, J.Y., Steenhuis, T.S., Li, L., Barry, D.A., Stagnitti, F., 2002. Column flow in stratified soils and fingers in Hele-Shaw cells: a review. Raats P. A. C., Smiles D., and Warrick A. W. (eds.). *Geophysical Monograph Series 129: Environmental mechanics: Water, Mass and Energy Transfer in the Biosphere*. American Geophysical Union, Washington, DC, pp. 79–85. <https://doi.org/10.1029/129GM08>.
- Rusanov, A.I., Esipova, N.E., Sobolev, V.D., 2019. Strong dependence of contact angle on pressure. *Dokl. Phys. Chem.* 487, 87–90. <https://doi.org/10.1134/S0012501619070017>.
- Sasidharan, S., Bradford, S.A., Šimůnek, J., Kraemer, S.R., 2019. Drywell infiltration and hydraulic properties in heterogeneous soil profiles. *J. Hydrol.* 570, 598–611. <https://doi.org/10.1016/j.jhydrol.2018.12.073>.
- Selker, J., Leclercq, P., Parlange, J.Y., Steenhuis, T., 1992a. Fingered flow in two dimensions: 1. Measurement of matric potential. *Water Resour. Res.* 28 (9), 2513–2521. <https://doi.org/10.1029/92WR00963>.
- Selker, J., Parlange, J.Y., Steenhuis, T., 1992b. Fingered flow in two dimensions: 2. Predicting finger moisture profile. *Water Resour. Res.* 28 (9), 2523–2528. <https://doi.org/10.1029/92WR00962>.
- Soto, D., Oaradelo, M., Corral, A., Periago, J.E.L., 2017. Pressure jumps during drainage in macroporous soils. *Vadose Zone J.* 16 (13), 1–12. <https://doi.org/10.2136/vzj2017.04.0088>.
- Sprenger, M., Leistert, H., Gimbel, K., Weiler, M., 2016. Illuminating hydrological processes at the soil-vegetation-atmosphere interface with water stable isotopes. *Rev. Geophys.* 54 (3), 674–704. <https://doi.org/10.1002/2015RG000515>.
- Spurin, C., Bultreys, T., Rücker, M., Garfi, G., Schlepütz, C.M., Novak, V., Berg, S., Blunt, M.J., Krevor, S., 2020. Real-time imaging reveals distinct pore-scale dynamics during transient and equilibrium subsurface multiphase flow. *Water Resour. Res.* 56 (12) <https://doi.org/10.1029/2020WR028287>.
- Starr, J.L., DeRoo, H.C., Frink, C.R., Parlange, J.Y., 1978. Leaching characteristics of a layered field soil. *Soil Sci. Soc. Am. J.* 42, 386–391. <https://doi.org/10.2136/sssaj1978.03615995004200030002x>.
- Steenhuis, T.S., Baver, C.E., Hasanpour, B., Stoof, C.R., DiCarlo, D.A., Selker, J.S., 2013. Pore scale consideration in unstable gravity driven finger flow. *Water Resour. Res.* 49 (11), 7815–7819. <https://doi.org/10.1002/2013WR013928>.
- Sun, Y., Kharaghani, A., Tsotsas, E., 2016. Micro-model experiments and pore network simulations of liquid imbibition in porous media. *Chem. Eng. Sci.* 150, 41–53. <https://doi.org/10.1016/j.ces.2016.04.055>.
- Sun, Z., Santamarina, J.C., 2019. Haines jumps: pore scale mechanisms. *Phys. Rev. E* 100, 023115. <https://doi.org/10.1103/PhysRevE.100.023115>.
- Tokunaga, T.K., Wan, J., 2001. Approximate boundaries between different flow regimes in fractured rocks. *Water Resour. Res.* 37 (8), 2103–2111. <https://doi.org/10.1029/2001WR000245>.
- Vereecken, H., Weihermüller, L., Assouline, S., Šimůnek, J., Verhoef, A., Herbst, M., Xue, Y., 2019. Infiltration from the pedon to global grid scales: an overview and outlook for land surface modeling. *Vadose Zone J.* 18 (1), 1–53.
- Wallach, R., Jortzick, C., 2008. Unstable finger-like flow in water-repellent soils during wetting and redistribution—the case of a point water source. *J. Hydrol.* 351 (1–2), 26–41. <https://doi.org/10.1016/j.jhydrol.2007.11.032>.
- Wallach, R., Margolis, M., Gruber, E.R., 2013. The role of contact angle on unstable flow formation during infiltration and drainage in wettable porous media. *Water Resour. Res.* 49 (10), 6508–6521. <https://doi.org/10.1002/wrcr.20522>.
- Wang, Z., Wallach, R., 2021. Water infiltration into subcritical water-repellent soils with time-dependent contact angle. *J. Hydrol.* 595, 126044 <https://doi.org/10.1016/j.jhydrol.2021.126044>.
- Wang, Z., Wallach, R., 2022. Modeling gravity-driven unstable flow in subcritical water-repellent soils with a time-dependent contact angle. *Water Resour. Res.* 58, e2021WR031859 <https://doi.org/10.1029/2021WR031859>.
- Wheeler, W.H., 1893. *Tidal rivers: Their (1) Hydraulics, (2) Improvement,(3) Navigation*. Longmans, Green and Company, p. 1893.
- Wijshoff, H., 2018. Drop dynamics in the inkjet printing process. *Curr. Opin. Colloid Interface Sci.* 36, 20–27.